tvst

Glaucoma

3D Reconstruction of a Unitary Posterior Eye by Converging Optically Corrected Optical Coherence and Magnetic Resonance Tomography Images via 3D CAD

Hyung Bin Hwang[1,2], Ji Su Yeon[3], Geo Seong Moon[3], Ha Na Jung[3], Jae Young Kim[3], Seung Hee Jeon[1,2], Joon Myoung Yoon[1,2], Hyo Won Kim[4], and Yong Chan Kim[1,2]

[1] Department of Ophthalmology, College of Medicine, The Catholic University of Korea, Seoul, Republic of Korea
[2] Department of Ophthalmology, Incheon St. Mary's Hospital, College of Medicine, The Catholic University of Korea, Seoul, Republic of Korea
[3] Idynamics, Seoul, Republic of Korea
[4] Gangnam St. Mary's One Eye Clinic, Seoul, Republic of Korea

Correspondence: Yong Chan Kim, Department of Ophthalmology, Incheon St. Mary's Hospital, College of medicine, The Catholic University of Korea, Republic of Korea, 56, Dongsu-ro, Bupyeong-gu, Incheon 21431, Republic of Korea.
e-mail: yongchankim@catholic.ac.kr

Received: February 3, 2022
Accepted: June 21, 2022
Published: July 27, 2022

Keywords: posterior eye; 3D reconstruction; CAD; MRI

Citation: Hwang HB, Yeon JS, Moon GS, Jung HN, Kim JY, Jeon SH, Yoon JM, Kim HW, Kim YC. 3D reconstruction of a unitary posterior eye by converging optically corrected optical coherence and magnetic resonance tomography images via 3D CAD. Transl Vis Sci Technol. 2022;11(7):24, https://doi.org/10.1167/tvst.11.7.24

Purpose: In acquiring images of the posterior eye, magnetic resonance imaging (MRI) provides low spatial resolution of the overall shape of the eye while optical coherence tomography (OCT) offers high spatial resolution of the limited range. Through the merger of the two devices, we attempted to acquire detailed anatomy of the posterior eye.

Methods: Optical and display distortions in OCT images were corrected using the Listing reduced eye model. The 3.0T orbital MRI images were placed on the three-dimensional coordinate system of the computer-aided design (CAD) program. Employing anterior scleral canal opening, visual axis, and scleral curvature as references, original and corrected OCT images were ported into the CAD application. The radii of curvature of the choroid–scleral interfaces (Rc values) of all original and corrected OCT images were compared to the MRI images.

Results: Sixty-five eyes of 33 participants (45.58 $\pm$ 19.82 years) with a mean Rc of 12.94 $\pm$ 1.24 mm on axial MRI and 13.66 $\pm$ 2.81 mm on sagittal MRI were included. The uncorrected horizontal OCT (30.51 $\pm$ 9.34 mm) and the uncorrected vertical OCT (34.35 $\pm$ 18.09 mm) lengths differed significantly from the MRI Rc values (both $P < 0.001$). However, the mean Rc values of the corrected horizontal (12.50 $\pm$ 1.21 mm) and vertical (13.05 $\pm$ 1.98 mm) images did not differ significantly from the Rc values of the corresponding MRI planes ($P = 0.065$ and $P = 0.198$, respectively).

Conclusions: Features identifiable only on OCT and features only on MRI were successfully integrated into a unitary posterior eye.

Translational Relevance: Our CAD-based converging method may establish the collective anatomy of the posterior eye and the neural canal, beyond the range of the OCT.

Introduction

Optical coherence tomography (OCT) has become a mainstay of clinical ophthalmology. OCT enables noninvasive cross-sectional imaging of internal ocular structures (such as the retinal nerve fiber layer) by measuring optical reflections.[1] An OCT system performs multiple longitudinal scans at a series of adjacent locations to create a two-dimensional map of reflective sites. Although it is often assumed that an OCT image shows the real anatomy of a structure, most commercial OCT platforms differ in terms of the image acquisition methodology and the image presentation mode. The A-scan paths commence at a node and spread fanwise, but the images are processed and

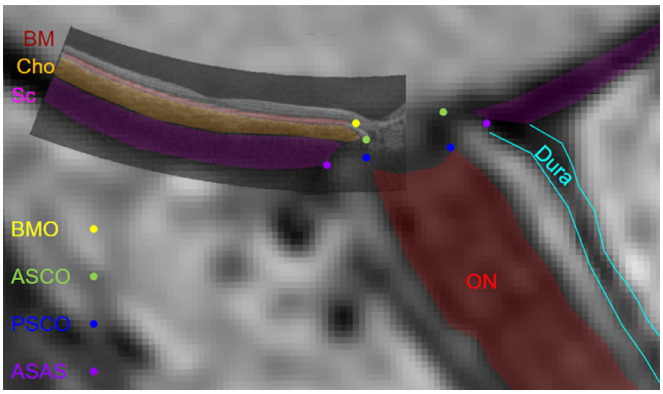

Figure 1. Merged OCT and MRI axial images. The Bruch's membrane (BM, *pink line*), choroid (Cho, *orange area*), sclera (Sc, *purple area*), and optic nerve parenchyme (ON, *red area*) are presented. BMO (*yellow dots*), ASCO (*green dots*), PSCO (*blue dots*), and ASAS (*purple dots*) are also presented.

presented in a rectangular format.[2] This fundamental geometric discrepancy between the physical scan paths and the presentation of results flattens the ocular curvature and compresses deep structures.[3] Correction of the distorted scan geometry remains challenging because A-scan progression varies individually.[3] The A-scan pupil entry angle is markedly affected by any aberration of the anterior segment and the κ angle-driven ocular alignment.[4] The location of the nodal point (the apex of the node) varies by the axial length (AXL).[5] Existing corrective approaches use optical estimations of common nodal points employing individual ocular biometric data derived using various eye models.[2,6] Reports have suggested that there are minimal differences in the radii of curvature yielded by corrected OCT and magnetic resonance imaging (MRI).[7,8] Thus, we hypothesized that the corrected-OCT posterior segment might serve as a surrogate when converging high-resolution but narrow-range OCT data into low-resolution but wide-range MRI information on the posterior eye. If so, the converged model could be used to identify OCT anatomic structures in the context of wide-ranging MRI. For example, OCT-identifiable features—such as the Bruch's membrane opening (BMO)—and features unidentifiable on OCT but identifiable on MRI—such as the mid-peripheral sclera, the scleral flange, and the optic nerve sheath—could be presented in a unitary manner (Figs. 1, 2). We thus developed a unitary ocular model by which to reconstruct the posterior eye by optically correcting the horizontal and vertical OCT curvatures and converging the corrected structure to that of the posterior MRI eye.

Methods

This was a single-center, retrospective case series. We used data from 65 eyes of 33 participants who underwent both MRI and ophthalmologic examinations in a tertiary general hospital (Incheon Saint Mary's Hospital, Incheon, Republic of Korea) between January 2018 and December 2021. The exclusion criteria were strabismus, retinal or choroidal disorders (such as diabetic retinopathy), retinal vascular diseases, age-related macular degeneration, poor-quality MRI or OCT scans, and any history of strabismus, vitreoretinal, glaucoma filtering, or tube

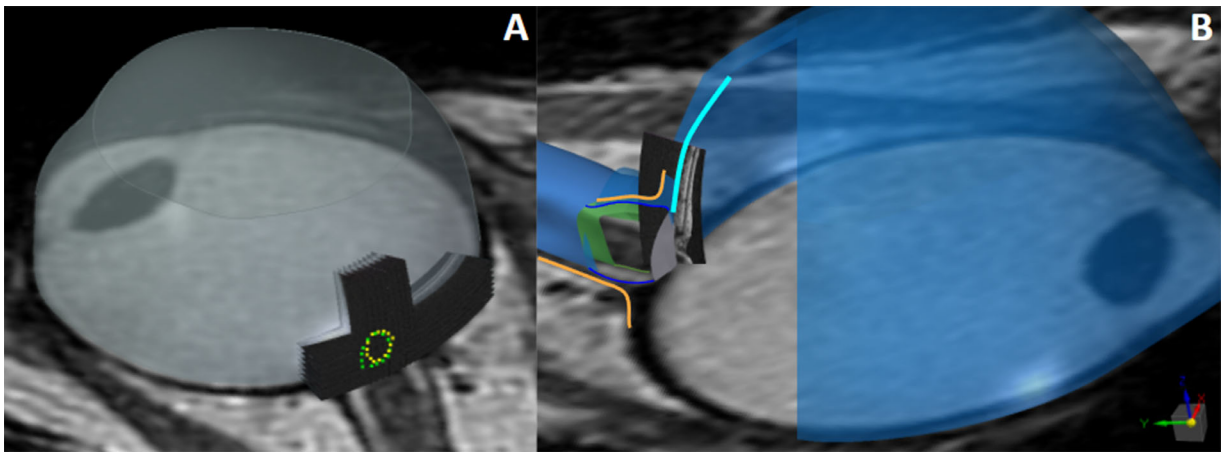

Figure 2. Reconstructed 3D model and sectional view. Features identifiable on OCT—the BMO, peripapillary sclera, and peripapillary atrophy—and features unidentifiable on OCT but identifiable on MRI—the mid-peripheral sclera, the scleral flange, the optic nerve sheath, and the optic nerve parenchyma—were integrated into a unitary posterior eye model. Inner sclera boundary (*sky blue solid line*), lamina cribrosa (*gray*), outer sclera boundary and dura outer (*orange solid line*), dura inner (*blue solid line*), and optic nerve parenchyma (*green*) are displayed.

surgery. The comprehensive ophthalmologic examination included evaluation of best-corrected visual acuity, tonometry, refraction, slit-lamp examination, dilated funduscopic examination, and ocular motility testing. AXL was measured via partial coherence interferometry (IOLMaster 500; Carl Zeiss Meditec, Zeiss Humphrey System, Dublin, CA, USA). The study was conducted in accordance with the ethical standards of the 1964 Declaration of Helsinki and was approved by The Catholic University of Korea Institutional Review Board (approval no. OC19RESI0161). Written informed consent was obtained from all participants.

MRI Image Acquisition and Processing

Orbital MRI images were acquired on the Ingenia CX 3.0-T (Philips Healthcare, Amsterdam, the Netherlands) platform. Each MRI image contained embedded information (in Dicom Tag format) on the relative positions, directions, and scales of all points relative to the reference coordinate system based in the center of the MRI scanner bore. The relative position of each point was presented as the X, Y, and Z components of the reference coordinate system with a scale (in millimeters) showing the number of image pixels (Fig. 3A). The axial scan that revealed the maximum

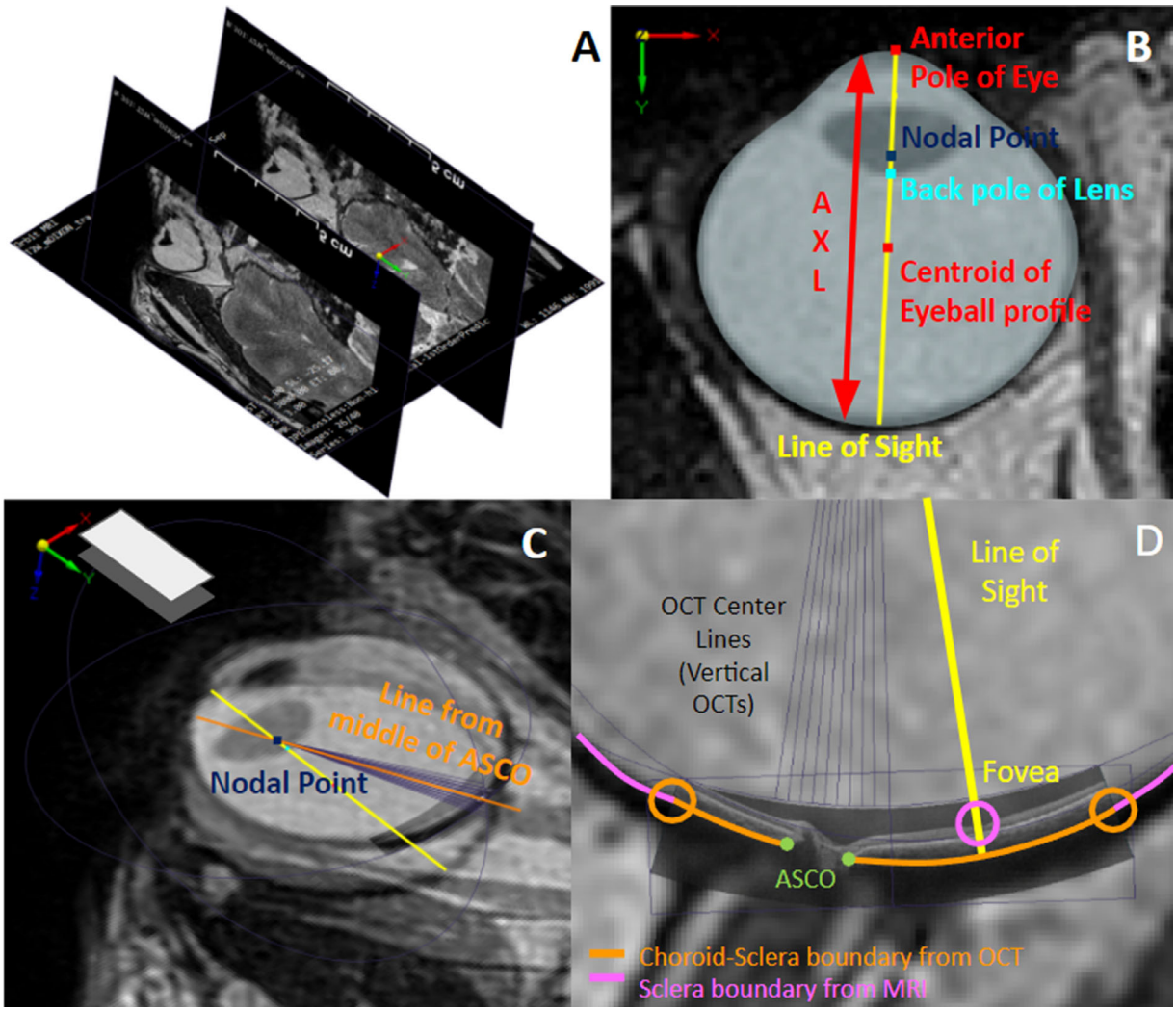

Figure 3. Concept of 3D reconstruction of a posterior eye by converging optically corrected OCT and MRI images. (A) MRI axial and sagittal scans were placed in the 3D space of the CAD program. (B) The linear line connecting the corneal apex (*red dot*) of the eye, the posterior pole (*light blue point*) of the lens, and the centroid of the eye (*red dot*) was assumed to be the visual axis. The AXL was measured from the anterior pole of the eye, back pole of the lens, and centroid of the eyeball. (C) In the frames showing the maximum transverse dimensions of the scleral canal and the surrounding optic nerve sheath, OCT image arrangement reference lines were drawn from the nodal point of the eye to the center of the ASCO of the neural canal (*orange line*). (D) The three points were considered when reviewing the consistency of MRI/OCT image overlap: continuity of the scleral boundary between MRI and OCT (*orange circle*), ASCO overlap between MRI and OCT (*green dot*), and whether the MRI visual axis passed through the fovea (*pink circle*).

transverse dimensions of the scleral shell was selected using the Moments algorithm of the 2015 Python Open Source Computer Vision Library; this was also used to estimate the centroid of the eye[9] (Fig. 3B). Each axial scan showing the maximum transverse dimensions of the scleral canal and the surrounding optic nerve sheath was manually identified by two independent observers (J.S.Y. and G.S.M.) (Fig. 3C). The axial scans were acquired with the (T2-weighted, fat-suppressed, repetition time (TR) = 3000 ms, echo time (TE) = 80 ms, field of view (FOV) = 150.588 mm, 512 × 512 pixels, 40 slices, resolution = 294 µm, slice thickness = 1 mm) parameters. The sagittal images were reconstructed from the multiple axial scans using a free software, 3D Slicer and Image Computing Platform of the Quantitative Imaging Network 2012 (http://www.slicer.org).[10]

Correction of Displayed OCT Images

OCTs were acquired using a Topcon swept-source device (DRIOCT Triton, Topcon Corporation, Tokyo, Japan) with an effective axial resolution of 8 µm, a central wavelength of 1050 nm, and an A-scan rate of 100,000/s. Inbuilt viewer software (Imagenet 6; Topcon Corporation) was used to display the horizontal and vertical scans to acquired eye volumes of 12.0 × 9.0 × 2.6 mm. All horizontal and vertical scans were downloaded at a 1:1 aspect ratio and edited into identical formats using freeware (GIMP, the GIMP Development Team, 2019; https://www.gimp.org).

As discussed above, OCT acquires images using a fan-beam light, but the images are processed and presented in rectangular format (Fig. 4A).[2] This flaws the ocular curvature.[3] Of the many models that estimate the position of the common nodal point, that of Kuo et al.[7] successfully corrected the OCT curvature using the Listing eye model. We thus calculated each nodal point as follows. Using the axial MRI scan showing the maximum transverse dimension of the scleral shell, we identified the visual axis and measured the AXL. The linear line connecting the corneal apex (red dot) of the eye, the posterior pole (light blue point) of the lens, and the centroid of the eye (red dot) was assumed to be the visual axis (Fig. 3B). As all light scans are assumed to share a common pivot at the nodal point of a (reduced) model eye, all points on a scanned retina were assumed to be equidistant to

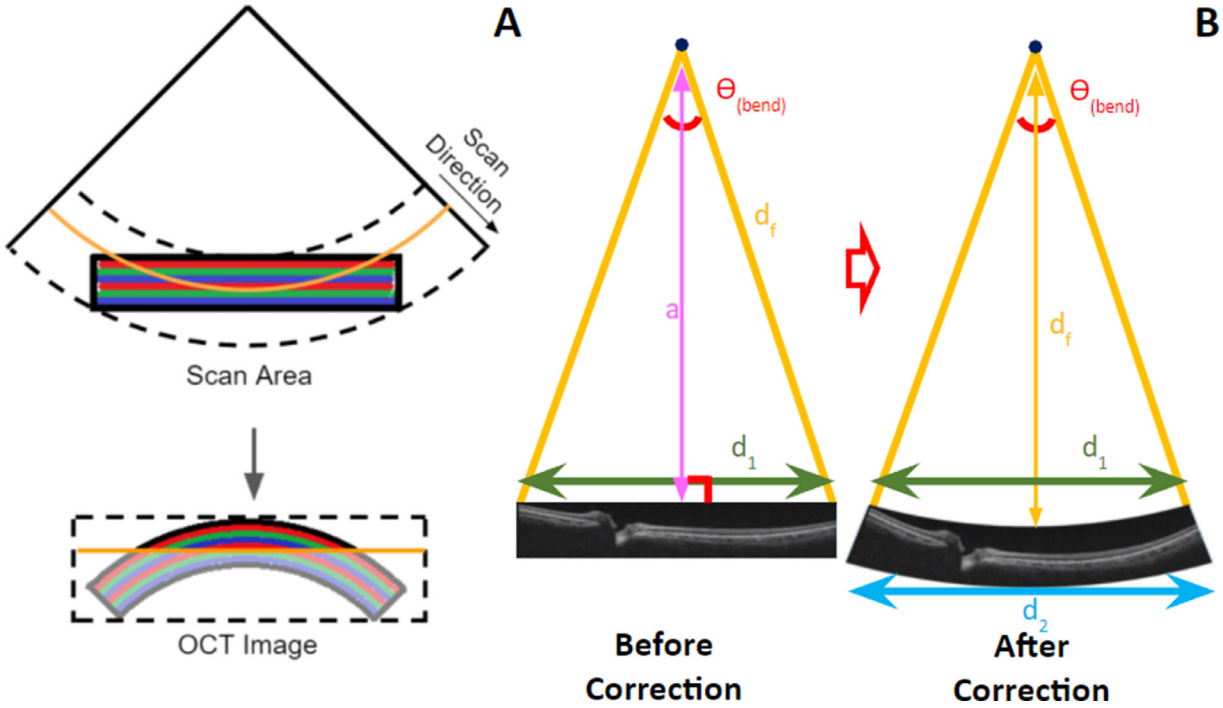

Figure 4. (A) Discrepancy between the scan paths and the presentation of OCTs. OCT acquires images using a fan-beam light, but the images are processed and presented in rectangular format. (B) As all light scans are assumed to share a common pivot at the nodal point of a reduced model eye, all points on a scanned retina were assumed to be equidistant to the nodal point (d_f). Also, the equidistant scan beam (d_f) can organize an equilateral triangle with a lower base (d_1) as the scan widths of the OCT. This triangle can also be organized into a right-angled triangle, which can be employed to a trigonometrical function. From these assumptions, the angle of the equilateral triangle (Θ_{bend}) can be calculated. The angle (Θ_{bend}) is used as the standard for bending the rectangular display of the OCT (uncorrected OCT) to a corrected OCT image that resembles the actual eye shape.

the nodal point (d_f in Fig. 4B). The Listing reduced eye exhibits a uniform refractive index of 1.336. For example, for a length of a 22.9-mm eye, the distance from the nodal point to the upper margin of scan beam is 17.14 mm, the distance from the nodal point to the principal point is 5.7 mm, and the (fictitious) refracting surface lies 1.5 mm behind the cornea.[11] From these assumptions, the distance from the nodal point to the upper margin of scan beam d_f is calculated as follows (Fig. 4B):

$$d_f = \frac{axial\ length\ of\ eye}{1.336}.$$

Also, under these assumptions, the equidistant scan beam (d_f) can organize an equilateral triangle with a lower base (d_1) as the scan widths of the OCT. This triangle can also be organized into a right-angled triangle, which can be employed to a trigonometrical function. From these assumptions, the angle of the equilateral triangle (Θ_{bend}) can be calculated as follow (Fig. 4B):

$$\theta_{bend} = 2 \times ArcSin\left(\frac{d_1}{2} \div d_f\right).$$

The angle (Θ_{bend}) is used as the standard for bending the rectangular display of the OCT (uncorrected OCT) to a corrected OCT image that resembles the actual eye shape (Fig. 4B). The manufacturer-reported scan widths (d_1) across the retina are 12 mm horizontally and 9 mm vertically.

Convergence of the MRI and OCT Images

A three-dimensional (3D) computer-aided design (CAD) program (Solid Edge ver. 220.0.0.104; Siemens Digital Industries Software, Munich, Germany) was used to converge MRI and OCT data. DICOM-type MRI images were converted to portable network graphics (PNG)-type images (the metadata were excluded to maintain anonymity). MRI axial and sagittal scans were placed in the 3D space of the CAD program using the location and scale information of the MRI DICOM Tags (DICOM TAG [0020, 0032] Image Position Patient and DICOM TAG [0020, 0037] Image Orientation Patient) (Fig. 3A). In the frames showing the maximum transverse dimensions of the scleral canal and the surrounding optic nerve sheath, OCT image arrangement (straight) reference lines were drawn from the nodal point of the eye to the center of the anterior scleral canal opening (ASCO) of the neural canal (orange line in Fig. 3C). The optically corrected horizontal and vertical OCT data of the optic disc were arranged around these reference lines, followed by four scans (at 0.35-mm intervals) from the top, bottom, left, and right of the primarily placed images (gray lines in Fig. 3D). An interval of 0.35 mm was chosen to reduce modeling errors caused by the difference in resolution between horizontal OCT (0.023 mm/pixel) and vertical OCT (0.035 mm/pixel). The following three points were considered when reviewing the consistency of MRI/OCT image overlap: continuity of the scleral boundary between MRI and OCT, ASCO overlap between MRI and OCT, and whether the MRI visual axis passed through the fovea (Fig. 3D).

Analysis of MRI/OCT Merging

We used certain measures to verify how accurately corrected OCT data represented structures near the neural canal compared to uncorrected data. The measures were (1) the scleral curvatures and thus the radii of curvature of the scleral boundary in the corrected and uncorrected OCT, as well as the MRI images. The scleral boundary (dotted pink curvature in Fig. 5) in an MRI image was approximated based on the inner edge of the ocular sclera, which was dark in T2-weighted images, and the scleral boundary in an OCT image, which was that of the sclera–choroid boundary within the image (green curvature in Fig. 5). Scleral curvatures were measured in axial and sagittal MRI reference sections, respectively. The uncorrected horizontal and vertical OCT distances and the corrected horizontal and vertical OCT distances were measured in the OCT reference scans (Fig. 5A). (2) The linear distances between the MRI and OCT scleral boundaries were measured at seven equidistant points (1.5 mm apart) based on the differences between the MRI curvature and those of uncorrected and corrected OCT (Fig. 5). OCT scleral curvatures anterior to the MRI curvature were positive, and OCT curvatures posterior to the MRI curvature were negative. (3) The reconstructed AXLs at the maximal linear distances between the anterior pole of the cornea on MRI scans and the corrected posterior pole on OCT scans and thus the longest distance inside the MRI-acquired scleral shell (red arrow in Fig. 3B). All measurements were performed using the inbuilt caliper of the CAD application, which is accurate to seven decimal points in millimeters, and were compared to the optical biometric measurements. Since the resolution of MRI and OCT differs significantly, the higher the dimensional precision, the more advantageous to match the common points of the two images accurately. Also, the intersubject variability of the measurements between the two observers is presented in Supplementary Table S1. All statistical analyses were conducted in R Studio (version 2021.09.1+372) (http://www.r-project.org/).

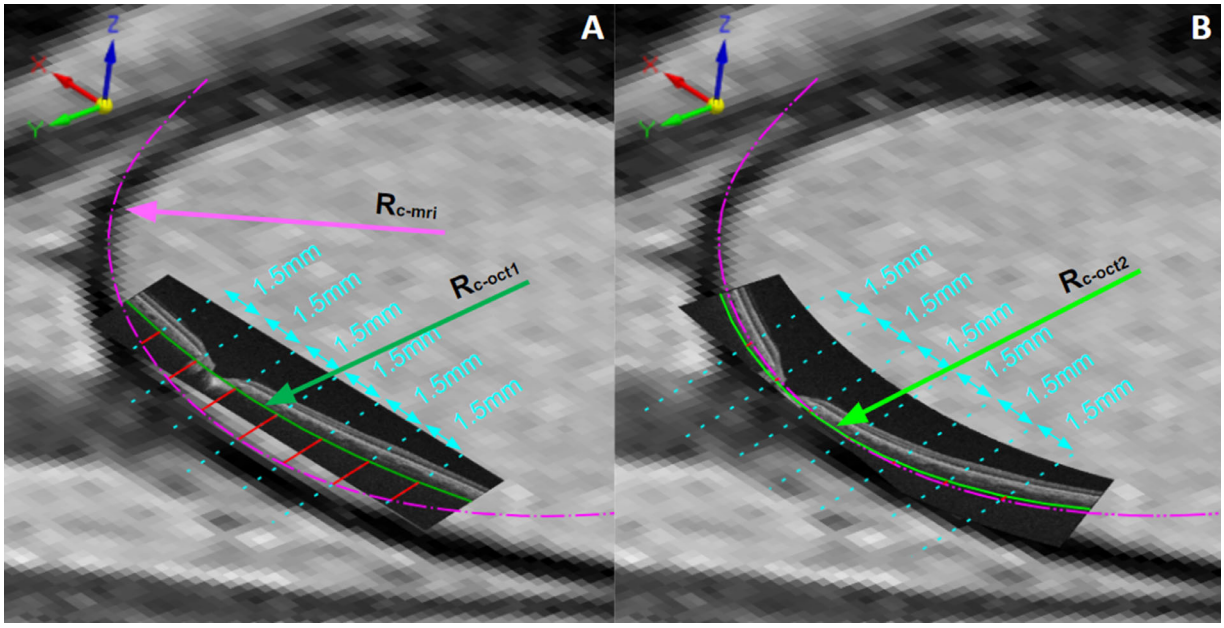

Figure 5. The radii of curvature of the scleral boundary in the uncorrected (Rc-OCT1), corrected OCT (Rc-OCT2), and the MRI (Rc-MRI) images. The linear distances between the MRI and OCT scleral boundaries were measured at seven equidistant points based on the differences between the MRI curvature and those of uncorrected and corrected OCT.

Results

In total, 136 eyes of 68 participants who underwent one or more OCT and/or MRI scans were included. All participants underwent OCT in our ophthalmology clinic because of suspected glaucoma. MRI scans were prescribed by our neurology or neurosurgery physicians, usually because a patient presented with symptoms of migraine. Seventy-one of 35 participants were excluded because of poor MRI resolution (14), poor-quality OCT (5), a history of optic neuropathy (7), glaucoma (4), a brain lesion (2), recent strabismus surgery (2), or congenital glaucoma (1). The final sample consisted of 65 eyes of 33 participants.

Table 1 summarizes the participants' demographics. The mean age at ophthalmologic examination was 45.58 ± 19.82 years, and the mean intraocular pressure was 16.13 ± 2.87 mm Hg. The AXL was measured via optical biometry and on the reconstructed ocular model using the CAD caliper. These mean AXLs were respectively 25.20 ± 1.89 mm and 25.17 ± 1.95 mm and thus not significantly different ($P = 0.710$) (Fig. 6). Figure 7 compares the scleral radii of curvature of MRI, uncorrected OCT, and corrected OCT. In the axial plane, the curvatures of MRI and the corrected OCT did not differ significantly (12.94 ± 1.24 mm and 12.50 ± 1.21 mm, respectively; $P = 0.065$). However, the axial curvatures of MRI and uncorrected horizontal OCT (30.51 ± 9.34 mm) differed greatly, accompanied by large individual deviations ($P < 0.001$). The MRI and corrected OCT curvatures in the sagittal plane did not differ significantly (13.66 ± 2.81 mm and 13.05 ± 1.98 mm, respectively; $P = 0.198$), but the sagittal curvatures of MRI and uncorrected OCT (34.35 ± 18.09 mm) were significantly different ($P < 0.001$).

Table 2 and Figure 8 show the scleral boundary differences between MRI and OCT in the axial and sagittal planes. The average difference between uncorrected horizontal OCT and axial MRI was signif-

Table 1. Demographics of Study Participants

Variable	Value
No. of participants (eyes)	33 (65)
Age, y	45.58 ± 19.82
Male/female, *n*	15/18
IOP, mm Hg	16.13 ± 2.87
Spherical error	−1.25 ± 3.05
Axial length, biometry, mm	25.20 ± 1.89
Axial length, MRI, mm	25.17 ± 1.95

Data are presented as mean ± standard deviation unless otherwise indicated. IOP, intraocular pressure.

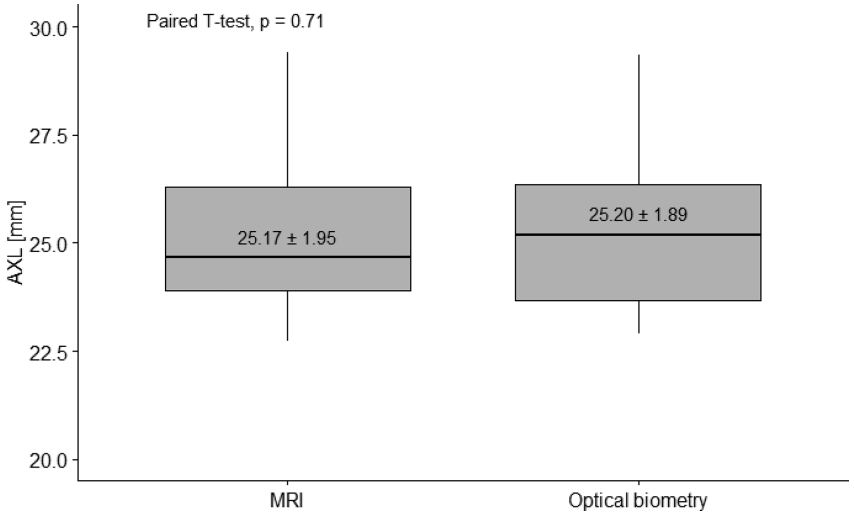

Figure 6. Comparison of the AXL measured with the optical biometry and with the reconstructed MRI images using the CAD caliper.

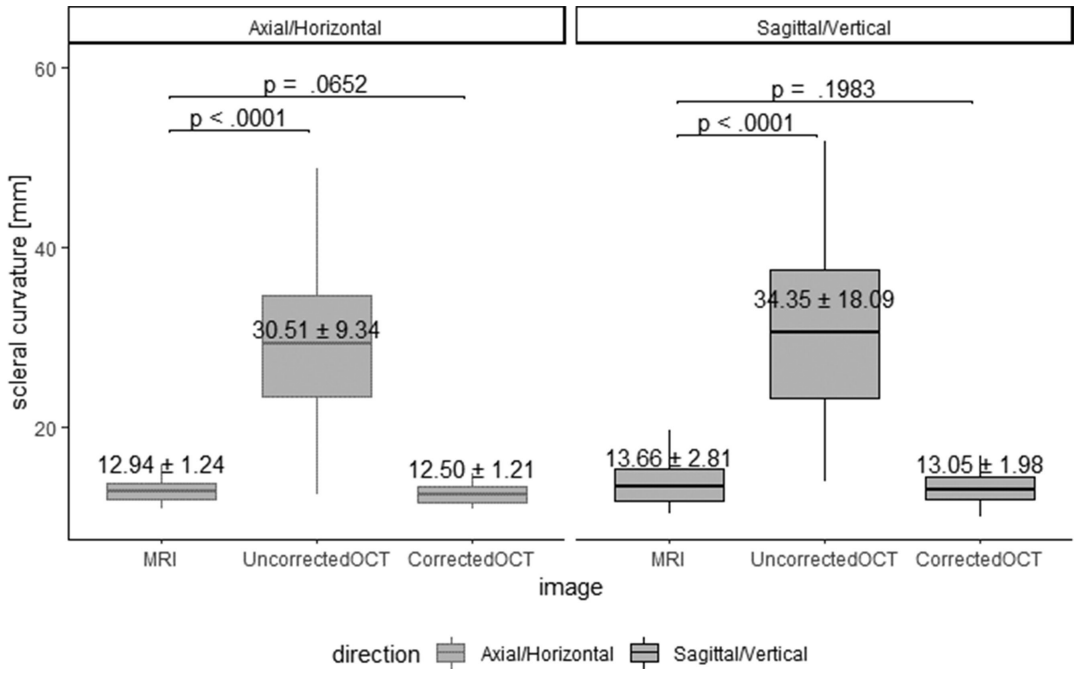

Figure 7. Comparison of the scleral radii of curvature of MRI, uncorrected OCT, and corrected OCT.

icantly larger than the average difference between corrected horizontal OCT and axial MRI ($P < 0.001$). The MRI/uncorrected OCT differences at all seven points (separated by 1.5 mm) were large (all $P < 0.001$). The MRI/corrected OCT scleral differences were rather similar at all seven points, but the MRI/uncorrected OCT difference was larger in the central part of the scan (positions 4 and 5). A similar trend was apparent in terms of the MRI/OCT scleral differences in the sagittal/vertical plane.

Discussion

We reconstructed the posterior eye using a 3D CAD application. We recognized the optical and display distortions of commercial OCT and corrected them via optical estimations of the nodal points. The corrected OCTs (both horizontal and vertical) were used to reconstruct a high-definition posterior eye by reference to the scleral canal. Features identifiable on OCT—the BMO, peripapillary sclera, and peripapillary atrophy—

Table 2. Scleral Boundary Differences Between Magnetic Resonance Tomography (MRIT) and OCT in the Axial and Sagittal Planes

		MRI–OCT Sclera Difference, mm							
MRI	OCT	1	2	3	4	5	6	7	Average
Axial	Uncorrected horizontal	−0.46 ± 0.34	−0.73 ± 0.33	−0.91 ± 0.31	−1.00 ± 0.31	−1.01 ± 0.31	−0.92 ± 0.31	−0.73 ± 0.33	−0.82 ± 0.27
	Corrected horizontal	0.19 ± 0.32	0.21 ± 0.29	0.20 ± 0.27	0.16 ± 0.26	0.11 ± 0.26	0.04 ± 0.30	−0.04 ± 0.34	0.13 ± 0.26
	P value[a]	**<0.001**	**<0.001**	**<0.001**	**<0.001**	**<0.001**	**<0.001**	**<0.001**	**<0.001**
Sagittal	Uncorrected vertical	−0.25 ± 0.31	−0.37 ± 0.31	−0.48 ± 0.33	−0.54 ± 0.34	−0.55 ± 0.35	−0.53 ± 0.36	−0.46 ± 0.38	−0.45 ± 0.32
	Corrected vertical	0.22 ± 0.30	0.19 ± 0.30	0.16 ± 0.30	0.13 ± 0.32	0.08 ± 0.32	0.05 ± 0.34	−0.01 ± 0.37	0.12 ± 0.30
	P value[a]	**<0.001**	**<0.001**	**<0.001**	**<0.001**	**<0.001**	**<0.001**	**<0.001**	**<0.001**

Data are presented as mean ± standard deviation unless otherwise indicated.

[a]Paired *t*-test between the uncorrected and the corrected images. Statistically significant values ($P < 0.05$) are shown in bold.

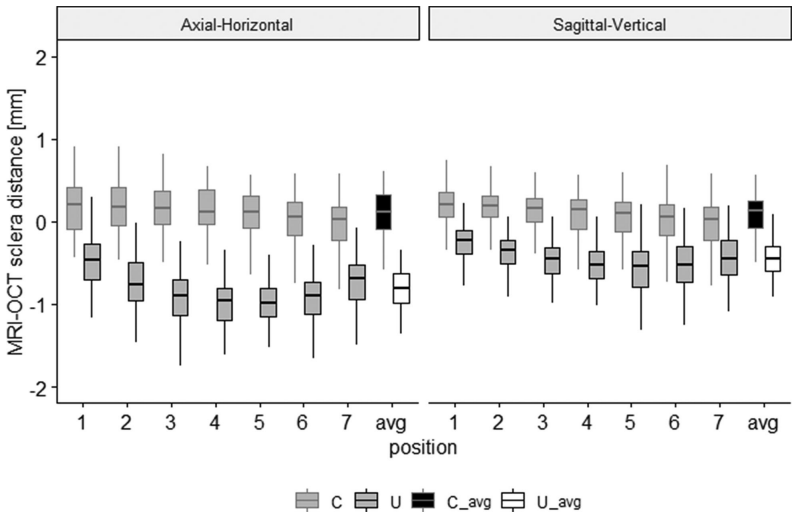

Figure 8. The scleral boundary differences between MRI and OCT in the axial and sagittal planes. The corrected and the uncorrected measures all had statistical difference, as shown in Table 2. C, corrected OCT versus MRI; C_avg, average difference of seven points of corrected OCT versus MRI; U, uncorrected OCT versus MRI; U_avg, average difference of seven points of uncorrected OCT versus MRI.

and features unidentifiable on OCT but identifiable on MRI—the mid-peripheral sclera, the scleral flange, the optic nerve sheath, and the optic nerve parenchyma—were integrated into a unitary model (Figs. 1, 2). We offer a conceptual framework for consideration of anatomic structures beyond the range of OCT, which is limited to routine observation.

OCT is now preferred for 3D ocular imaging in ophthalmology clinics and research centers worldwide.[12,13] Although the fan-beam scan distorts the images, application of the values output by commercial OCT software is acceptable for the following reasons. First, the retinal layer thicknesses are direct A-scan distances; measures further from the beam center are thicker. Second, the scan proceeds around a point centered on the anatomic location of interest, such as the macula or the optic disc. Third, most commercial OCT software averages the retinal layer thickness by region, mitigating the error associated with the first point above. However, when measuring the curvature of a wide area, the error increases as the measurement range increases. We found that the scleral curvatures were substantially distorted both horizontally and vertically in the original OCT displays. Using the radius of curvature as a surrogate of ocular shape, the eye shape in the corrected OCT images was much closer to that of the reference technique (MRI) and to the published values of posterior eye curvature.[7] Also, ocular curvature was far less variable in corrected images than in uncorrected images.

Our method should increase our understanding of the neural canal as a whole. The eye shape of individuals with myopia differs from that of emmetropic individuals; certain eye shapes are associated with a poor visual prognosis.[14,15] Most studies to date on

associations of eye shape with myopia prognosis have used MRI to observe changes in the posterior eye.[16,17] MRI offers full penetration of the region of interest, but the resolution is limited to 500 µm; commercial OCT devices afford much higher resolution but much less penetration. The resolution/penetration gaps of the two modalities render it difficult to integrate the scientific discoveries of various clinical studies that use different devices.[18,19] For example, Hong et al.[20] recently used OCT-measured parameters to explore the geometry of the neural canal; it was suggested that increased temporal displacement of the BMO compared to the ASCO was a prominent feature of highly myopic eyes.[21] The BMO and ASCO extend to the deeper structures, including the posterior scleral canal opening (PSCO) and the most anterior aspect of the subarachnoid space (ASAS), which should be considered unitary structures when studying changes in the neural canal.[22] Several reports have suggested that the temporal side of the optic nerve sheath experiences most of the biomechanical stress during ocular adduction, perhaps because the length redundancy of the normally sinuous optic nerve sheath has become exhausted, thus stretching and deforming the globe and the neural canal.[23–25] That canal extends to the peripapillary sclera and the optic nerve sheath; careful inspection of these structures is essential when investigating changes, especially when the primary causes of such changes are assumed to lie in structures of the deep neural canal or the outer sclera. We plan to investigate the relationships between OCT-measured parameters and otherwise measured parameters of the reconstructed deep neural canal, such as the PSCO and the ASAS.

Our reconstruction method using CAD affords several advantages when converging the two different types of ocular images. Humans exhibit cognitive limitations when operating in 3D space, especially when dealing with two or more objects. The 3D CAD program features unique algorithms that handle this problem, porting various images created using multiple coordinate systems to a single reference coordinate system. This merges different image types by reference to their geometries in 3D space. The stacked OCT images were merged in an orderly manner with the reconstructed MRI data. Also, the 3D CAD program uses a basic spline curve to facilitate the generation of curves containing aggregated points in 3D space. These attributes render the program appropriate when accurately reconstructing the curves of the posterior eye. The advanced curve-processing features measure the posterior sclera curvatures in various regions, which are usually derived subjectively.[16,26,27] In addition, the program measures not only one-dimensional linear distances and radii but also the volumes, surface areas, and volume centers of complex curved surfaces and structures, which are essential when reconstructing the multidimensional ocular structure. The measurement accuracy extends to seven decimal points. Finally, CAD modeling facilitates subsequent studies using finite element methods (FEMs). The model serves as the basis for FEM mesh generation and supports most storage formats used by analyses that exploit FEMs.

Our work had certain limitations. First, nonoptical MRI imaging is associated with inaccuracies in resolution limits and also magnetic gradient field nonlinearities and magnetic field inhomogeneities.[28] The latter two inaccuracies are of particular concern in areas evidencing large differences in magnetic susceptibilities, such as the anterior eye.[29] Our 3D MRI volume acquisitions were centered on the posterior eye; this reduced errors. Second, the correction algorithms that we used do not consider the magnification errors corrected using the Littmann formula.[30] However, the latter does not correct image shape; our method corrects the optical paths of both the system and the eye and thus simultaneously adjusts both the magnification and the shape. Our use of the Listing eye model was based on a previous report that successfully used this algorithm to correct the shapes of OCT images.[7] Third, we could not convert the original sagittal MRI images, rather only reconstructed images from the axial scans. As time elapses between an axial and a sagittal scan, the patient's posture changes. The limited resolution of reconstructed sagittal images renders it difficult to accurately measure the deep neural canal; the use of original sagittal images would have been preferable. Fourth, our model eye assumed that the visual and the optical axes coincided, which is not the case.[4] Although the macular position was based on these assumptions, convergence was based largely on the continuity of the scleral boundary between MRI and OCT images and the overlap agreement revealed by ASCO. We considered the κ angle and used the visual axis to broadly outline the fovea. We combined the high-resolution OCT area with the wide-imaging MRI region; we plan to inspect the deep neural canal. Fifth, the OCT image was corrected while drawing an arc of the same radius from the nodal point, following the assumption of the Listing reduced eye model. However, the actual shape of the eyeball is different from the Listing reduced eye, and also the position of the nodal point may not be as constant. However, the results of Kuo et al.[7] show that the error between the actual ray that arrives in the eye (analytical correction) and the estimation using the reduced model (numerical correction) is roughly 0.3 mm in radial

curvature. We also have calculated d_1 lateral distortion for an average AXL of eyes in our analysis (Supplementary Fig. S1). The positions of the outermost point (purple point) in the uncorrected OCT and the outermost point (green) in the corrected OCT image are displayed. For a horizontal scan of 12 mm, lateral distortion is 0.28 mm, which is only 4.67% of horizontal length, which is not expected to have a significant effect on the measured value.

Prior studies using MRI to observe and measure the structure of the sclera have been conducted by a number of researchers, including uses of the latest high-magnetic field MRI.[31] Langner et al.[32] measured the anterior segment of the eye using a 7.1T MRI scanner, and Nguyen et al.[33] measured the optic nerve area and BMO area with a 7.0T whole-body scanner. Along with the improvement of resolution, research on the measurement techniques was also conducted. Ho et al.[34] introduced magic angle-enhanced MRI techniques in images observed in a 9.4T horizontal MRI scanner to show that the observation of subvoxel microstructures can be improved. Voorhees et al.[35] used subpixel measurement techniques in images observed in the 9.4T horizontal MRI scanner to measure the deformation of the whole-globe and optical nerve head according to IOP changes. In this study, a 3.0T orbital MRI was used, but as in the case of aforementioned studies, it seems possible to establish an eye structure model with improved precision through the use of high magnetic field MRI and magic angle-enhanced technique.

We describe a method by which to reconstruct the posterior eye by converging optically corrected OCT images with orbit MRI images using a 3D CAD program. This enables identification of anatomic OCT structures in the wide-range MRI context. We offer a conceptual framework for consideration of the anatomic structures beyond the range of OCT that is now clinically routine.

Acknowledgments

Supported by a Grant of Translational R&D Project through the Institute for Bio-Medical Convergence, Incheon St. Mary's Hospital, The Catholic University of Korea.

Disclosure: **H.B. Hwang**, None; **J.S. Yeon**, None; **G.S. Moon**, None; **H.N. Jung**, None; **J.Y. Kim**, None; **S.H. Jeon**, None; **J.M. Yoon**, None; **H.W. Kim**, None; **Y.C. Kim**, None

References

1. Huang D, Swanson EA, Lin CP, et al. Optical coherence tomography. *Science*. 1991;254:1178–1181.
2. Podoleanu A, Charalambous I, Plesea L, Dogariu A, Rosen R. Correction of distortions in optical coherence tomography imaging of the eye. *Phys Med Biol*. 2004;49:1277–1294.
3. Chen M, Gee JC, Prince JL, Aguirre GK. 2D modeling and correction of fan-beam scan geometry in OCT. *Comput Pathol Ophthalmic Med Image Anal (2018)*. 2018;11039:328–335.
4. Berrio E, Tabernero J, Artal P. Optical aberrations and alignment of the eye with age. *J Vis*. 2010;10(14):34.
5. Snead MP, Hardman Lea S, Rubinstein MP, Reynolds K, Haworth SM. Determination of the nodal point position in the pseudophakic eye. *Ophthalmic Physiol Opt*. 1991;11:105–108.
6. Westphal V, Rollins A, Radhakrishnan S, Izatt J. Correction of geometric and refractive image distortions in optical coherence tomography applying Fermat's principle. *Opt Express*. 2002;10:397–404.
7. Kuo AN, McNabb RP, Chiu SJ, et al. Correction of ocular shape in retinal optical coherence tomography and effect on current clinical measures. *Am J Ophthalmol*. 2013;156:304–311.
8. Verkicharla PK, Suheimat M, Pope JM, et al. Validation of a partial coherence interferometry method for estimating retinal shape. *Biomed Opt Express*. 2015;6:3235–3247.
9. Clark RA, Demer JL. Differential lateral rectus compartmental contraction during ocular counterrolling. *Invest Ophthalmol Vis Sci*. 2012;53:2887–2896.
10. Fedorov A, Beichel R, Kalpathy-Cramer J, et al. 3D Slicer as an image computing platform for the Quantitative Imaging Network. *Magn Reson Imaging*. 2012;30:1323–1341.
11. Katz M. *The Human Eye as an Optical System*. Philadelphia: Harper & Row; 1979.
12. Brar M, Yuson R, Kozak I, et al. Correlation between morphologic features on spectral-domain optical coherence tomography and angiographic leakage patterns in macular edema. *Retina*. 2010;30:383–389.
13. Park HY, Park CK. Diagnostic capability of lamina cribrosa thickness by enhanced depth imaging and factors affecting thickness in patients with glaucoma. *Ophthalmology*. 2013;120:745–752.
14. Kim YC, Chang DJ, Park SJ, et al. Machine learning prediction of pathologic myopia using

tomographic elevation of the posterior sclera. *Sci Rep*. 2021;11:6950.
15. Ohno-Matsui K, Jonas JB. Posterior staphyloma in pathologic myopia. *Prog Retin Eye Res*. 2019;70:99–109.
16. Moriyama M, Ohno-Matsui K, Hayashi K, et al. Topographic analyses of shape of eyes with pathologic myopia by high-resolution three-dimensional magnetic resonance imaging. *Ophthalmology*. 2011;118:1626–1637.
17. Guo X, Xiao O, Chen Y, et al. Three-dimensional eye shape, myopic maculopathy, and visual acuity: the Zhongshan Ophthalmic Center-Brien Holden Vision Institute High Myopia Cohort Study. *Ophthalmology*. 2017;124:679–687.
18. Kim YC, Jung KI, Park HL, Park CK. Three-dimensional evaluation of posterior pole and optic nerve head in myopes with glaucoma. *Sci Rep*. 2017;7:18001.
19. Kim YC, Koo YH, Jung KI, Park CK. Impact of posterior sclera on glaucoma progression in treated myopic normal-tension glaucoma using reconstructed optical coherence tomographic images. *Invest Ophthalmol Vis Sci*. 2019;60:2198–2207.
20. Hong S, Yang H, Gardiner SK, et al. OCT-detected optic nerve head neural canal direction, obliqueness and minimum cross-sectional area in healthy eyes. *Am J Ophthalmol*. 2019;208:185–205.
21. Jeoung JW, Yang H, Gardiner S, et al. Optical coherence tomography optic nerve head morphology in myopia I: implications of anterior scleral canal opening versus Bruch membrane opening offset. *Am J Ophthalmol*. 2020;218:105–119.
22. Yang H, Downs JC, Girkin C, et al. 3-D histomorphometry of the normal and early glaucomatous monkey optic nerve head: lamina cribrosa and peripapillary scleral position and thickness. *Invest Ophthalmol Vis Sci*. 2007;48:4597–4607.
23. Demer JL. Optic nerve sheath as a novel mechanical load on the globe in ocular duction. *Invest Ophthalmol Vis Sci*. 2016;57:1826–1838.
24. Wang X, Beotra MR, Tun TA, et al. In vivo 3-dimensional strain mapping confirms large optic nerve head deformations following horizontal eye movements. *Invest Ophthalmol Vis Sci*. 2016;57:5825–5833.
25. Suh SY, Le A, Shin A, Park J, Demer JL. Progressive deformation of the optic nerve head and peripapillary structures by graded horizontal duction. *Invest Ophthalmol Vis Sci*. 2017;58:5015–5021.
26. Lee KM, Park SW, Kim M, Oh S, Kim SH. Relationship between three-dimensional magnetic resonance imaging eyeball shape and optic nerve head morphology. *Ophthalmology*. 2021;128:532–544.
27. Ohno-Matsui K. Proposed classification of posterior staphylomas based on analyses of eye shape by three-dimensional magnetic resonance imaging and wide-field fundus imaging. *Ophthalmology*. 2014;121:1798–1809.
28. Wang D, Strugnell W, Cowin G, Doddrell DM, Slaughter R. Geometric distortion in clinical MRI systems part I: evaluation using a 3D phantom. *Magn Reson Imaging*. 2004;22:1211–1221.
29. Sumanaweera TS, Adler JR, Jr, Napel S, Glover GH. Characterization of spatial distortion in magnetic resonance imaging and its implications for stereotactic surgery. *Neurosurgery.* 1994;35:696–703.
30. Bennett AG, Rudnicka AR, Edgar DF. Improvements on Littmann's method of determining the size of retinal features by fundus photography. *Graefes Arch Clin Exp Ophthalmol*. 1994;232:361–367.
31. Boote C, Sigal IA, Grytz R, Hua Y, Nguyen TD, Girard MJA. Scleral structure and biomechanics. *Prog Retin Eye Res*. 2020;74:100773.
32. Langner S, Martin H, Terwee T, et al. 7.1 T MRI to assess the anterior segment of the eye. *Invest Ophthalmol Vis Sci*. 2010;51:6575–6581.
33. Nguyen BN, Cleary JO, Glarin R, et al. Ultra-high field magnetic resonance imaging of the retrobulbar optic nerve, subarachnoid space, and optic nerve sheath in emmetropic and myopic eyes. *Transl Vis Sci Technol*. 2021;10:8.
34. Ho LC, Sigal IA, Jan NJ, et al. Non-invasive MRI assessments of tissue microstructures and macromolecules in the eye upon biomechanical or biochemical modulation. *Sci Rep*. 2016;6:32080.
35. Voorhees AP, Ho LC, Jan NJ, et al. Whole-globe biomechanics using high-field MRI. *Exp Eye Res*. 2017;160:85–95.